


Article

Tightly Coupled Ultra-Wideband Phased-Array Implemented by Three-Dimensional Inkjet Printing Technique

Lei Han ^{1,2}, Gang Wang ¹, Lin Zhang ¹, Weixu Jiang ², Pengbing Zhao ³, Wei Tang ², Tao Dang ² and Hongxing Zheng ^{4,*} 

¹ Department of Air-Defense and Anti-Missile, Air Force Engineering University, Xi'an 710100, China

² Sichuan Jiuzhou Electric Group Co., Ltd., Mianyang 621000, China

³ School of Electro-Mechanica Engineering, Xidian University, Xi'an 710071, China

⁴ School of Electronics and Information Engineering, Hebei University of Technology, Tianjin 300401, China

* Correspondence: hxzheng@hebut.edu.cn; Tel.: +86-22-6043-8244

Abstract: In order to enhance the gains from antennas suitable for airplane-mounted platforms, a tightly coupled antenna array is investigated in this paper. Specifically, a three-dimensional (3-D) inkjet printing technique is used to implement the conformal characteristics needed for the array. Both the radiators and substrate of the antenna array have been fabricated by combining the fused deposition modeling and microdroplet injection molding technologies, based on an existing 3-D printer. Here, through a unique combination of 3-D and 2-D inkjet printing of dielectric material and metallic ink, respectively, we demonstrate a monolithically integrated design for a nonplanar antenna for the first time. The antenna measurements herein show the complete characterization of this new process in terms of minimum feature size and achievable conductivities. This antenna configuration offers a high-gain performance with a low-cost and rapid fabrication technique by using 3-D printing techniques. To check our design, the voltage standing wave ratio and radiation patterns were tested after adding the newly designed feed structure. The results show that the design process is very efficient. Both the antenna element and the array demonstrate positive properties and are in very good agreement with the specially mounted platform.

Keywords: ultra-wideband; conformal antenna array; tightly coupled antenna; three-dimensional printing technique; fused deposition modeling; microdroplet injection molding



Citation: Han, L.; Wang, G.; Zhang, L.; Jiang, W.; Zhao, P.; Tang, W.; Dang, T.; Zheng, H. Tightly Coupled Ultra-Wideband Phased-Array Implemented by Three-Dimensional Inkjet Printing Technique. *Electronics* **2022**, *11*, 3320. <https://doi.org/10.3390/electronics11203320>

Academic Editors: Mohammad Maktoomi, Tutku Karacolak, Mohamed Helaoui, Syed Azeemuddin and Giovanni Andrea Casula

Received: 5 September 2022

Accepted: 12 October 2022

Published: 14 October 2022

Publisher's Note: MDPI stays neutral with regard to jurisdictional claims in published maps and institutional affiliations.



Copyright: © 2022 by the authors. Licensee MDPI, Basel, Switzerland. This article is an open access article distributed under the terms and conditions of the Creative Commons Attribution (CC BY) license (<https://creativecommons.org/licenses/by/4.0/>).

1. Introduction

Tightly coupled antenna arrays represent one of the most important techniques in the field, due to their many attractive features, such as high gain, wide bandwidth, and the ability to radiate in both omnidirectional and directive patterns [1]. Due to their compact size, this type of array has been attracting more and more research interest. Ben Munk proposed an ultra-wideband (UWB) phased antenna array based on the strong coupling effect between elements [2]. This is the first time that a design method was proposed that is fundamentally different from the traditional phased array technology. Its core idea was to intentionally increase the mutual coupling between elements in the array [3], and the authors successfully developed an ultra-wideband 2 GHz–18 GHz phased array antenna prototype using this mechanism. Due to their unique advantages, more studies of tightly coupled ultra-wideband phased arrays based on this mechanism were subsequently conducted [4,5]. The fabrication technology has also received much research attention.

With the development of wireless equipment miniaturization, a redesign of the packaging of the circuits and sensors embedded in conformal array antennas and electronic components was also required [6]. The gains of the antenna array can be increased by adding a number of elements. However, the gain is not linearly proportional to the number of elements, and after many elements have been added, the size of the array is greatly increased and limits its use in the space. Recently, a UWB tightly coupled phased array

covering 1.2 GHz–6 GHz has been proposed, which is conformed on a cylindrical carrier and can scan up to 60° along the circumferential direction [7]. Although this antenna has achieved much in terms of bandwidth and large-angle scanning, when the antenna is only arranged according to a cylindrical shape, its array is relatively regular and there has not been any breakthrough in the conformation of the antenna; therefore, it is still a static-planar dipole antenna. Based on a Marchand balun and a double-layered frequency selection surface (FSS) structure, a tightly coupled antenna array with $\pm 60^\circ$ angle scanning was archived in the bandwidth of 2–18 GHz [8]; its profile height was only 0.1λ at the lowest operating frequency. Later, several tight-coupled arrays with a lower profile that are more suitable for this type of conformation were reported [9,10]. However, these antennas have been designed independently without considering the mounted platform. In order to obtain a better performance, the conformal antenna array process is becoming more and more precise, along with the development of mechanism fabrication. The array must be considered along with the mounted platform at the same time during the design process. In the current study, the most challenging problem is the antenna design; it is more difficult for us to fabricate the antenna to meet the specific mounting requirements.

In order to marry with the mounted platform, three-dimensional (3-D) printing technology for the antenna design and fabrication was chosen. The idea of mechanism fabrication using 3-D printing technology originated with a topographic map of a layered structure and was promoted and developed later [11]. With the current computer-aided design and manufacturing technology, the development direction of equipment printed using 3-D printing technology has gradually moved from a single homogeneous material to heterogeneous multi-materials, from single to multiple processes, and from a flat plane to curved surfaces. Traditional 3-D printing technology involves a complex model that is sliced and then reduced to a flat graphic layout. While putting a patch on the surface of the object to complete the total piece [12], conformal printing techniques have been implemented in the mechanism fabrication. However, to implement a smart control device, a conformal printed electronic circuit on a mechanical structure's surface is required, such as a circuit embedded in a sensor to implement mechanic-electronic co-fabrication. Recently, Paulsen J. et al., combined 3-D printing and aerosol spray technologies to fabricate embedded circuits and sensors [13]. Kim used lead-based alloys with low melting points and additive manufacturing techniques to study the fabrication of printed circuit boards (PCBs) [14]. Muth et al. studied embedded 3-D printing to prepare stretchable and, at the same time, conformal circuits and sensors with better performance [15]. These techniques are better suited for the circuits' fabrication. In some cases, the conformal antenna is always required to meet the surface of the object. However, conformal printing has been less commonly reported for antennas.

The technology behind 3-D printing uses an additive process that reduces material wastage; by using a digitally controlled method, the machine deposits a precise amount of material at a desired location. However, these structures usually require integrated metal and dielectric components, and current inkjet printing technology is still immature in depositing dielectric and metal components at the same time. Inkjet printing using only dielectric materials has previously been used to fabricate structures [16,17]. Elsewhere, inkjet printing using only metals has been employed to fabricate antennas on conventional planar substrates [18,19]. There are currently not many reports that show the integration of inkjet-printed metal and dielectric components to realize a structure. Other deposition methods, such as spraying and painting, have been used for the metallization of 3-D printed dielectrics [20,21]. These methods are manual, with less control over material deposition and layer thickness; hence, they cause significant material wastage. They are also not suitable for large-volume manufacturing. Here, a unique combination of inkjet printing with dielectric and metal materials has been utilized for the realization of a novel 3-D antenna configuration.

In this approach, a conformal antenna based on the tightly coupled antenna principle is designed. The feasibility of 3-D technology, combined with a tightly coupled ultra-

wideband antenna, is investigated in detail; the substrate and radiator of the antenna are fabricated using the 3-D printing technique. For the first time, a tightly coupled antenna has been monolithically integrated into a dielectric mounted platform via inkjet printing technology. As a result of conformal integration, a tightly coupled antenna array provides a peak gain of 12.9 dBi in the X-band. The characterization of the inkjet-printed 3-D dielectric material, as well as inkjet-printed metal, on this dielectric in terms of minimum feature sizes and conductivities has also been reported. This work shows the advantages of conformal inkjet-printing technology, which has heretofore been limited to planar antenna design procedures and can easily be integrated into a structure with a convex shape. A fabricated sample has been measured, and the results are in very good agreement with the simulation.

The rest of the paper is organized as follows. The relationship between the elements of the tightly coupled array is analyzed in Section 2. A butterfly-shaped symmetric radiation unit is designed as a basic structure of the phased-array. By using high-frequency simulation system (HFSS) software, the modeling antenna is first analyzed and then optimized. After simulation, the performance index of the antenna element is described in Section 3. In terms of a conformal prototype of the tightly coupled antenna array, the properties of the 3-D printer are analyzed in Section 4, where the key techniques of the printing process are described in detail. The appropriate parameters of the 3-D printer can be found in this section. To obtain an excellent performance from the array, the feed structure has been designed and will be discussed in Section 5. Finally, the experimental results have been obtained and will be discussed in Section 6, then we offer our conclusions in Section 7.

2. Antenna Element Structure Design

The radiation part is the basic element of the antenna array, and it is also a key component of the coupling relationship between the array elements of the tightly coupled array. Therefore, the design of a tightly coupled radiation element becomes the most important research task with a tightly coupled array. To design a broadband antenna element, the most common method is to choose a radiation body form and size with a broadband property. A traveling wave antenna and non-frequency variative antenna comprise the two main options. The former is based on current distribution without reflection, and with a very wide input impedance characteristic; the latter essentially means that the antenna structure does not change with the electrical length. The input impedance and directional characteristic of both are broadband. The design of a tightly coupled radiation element is completely different from that of a conventional element, and introduces a strong coupling effect between each element of the array. This is mainly because with an increase in the impedance bandwidth of the array, the designer has to introduce an additional capacitance to offset the inductive effect raised by the reflective ground. A short dipole with an overlapping structure at the end of the adjacent elements is used as the array element, which can effectively widen the antenna's working frequency band. The short dipole elements are connected at the beginning and end, and the element spacing is much smaller, which can strengthen the coupling effect between elements. The overlapping structure at the end forms a coupling capacitance that can be used to offset the inductive effect of the reflective ground.

The basic principle of a tightly coupled antenna is shown in Figure 1. The h variable in the figure indicates the distance between the tightly coupled antenna element and the metal ground, the ZTCDA indicates the input impedance of a tightly coupled antenna element in an infinite array with the metal ground, R_{A0} and X_A indicate the radiation resistance and radiation reactance of the tightly coupled antenna element in the infinite array without the metal ground, respectively, and Z_+ represents the impedance when looking from the antenna plane to the metal ground. Therefore, in this array, the radiation impedance of the tightly coupled antenna element in the absence of the metal ground can be expressed as:

$$Z_{A0} = R_{A0} + jX_A. \quad (1)$$

Z_{1+} can be considered as the equivalent transmission line impedance of a shorted section of termination; this can be expressed as:

$$Z_{1+} = j2R_{A0} \tan(\beta h) \tag{2}$$

where β is the propagation constant in free space. When the antenna is added to the metal ground, the total input impedance of the tightly coupled antenna is expressed as:

$$Z_{TCDA} = jX_A + 2R_{A0}(j2R_{A0} \tan(\beta h)) / (2R_{A0} + j2R_{A0} \tan(\beta h)). \tag{3}$$

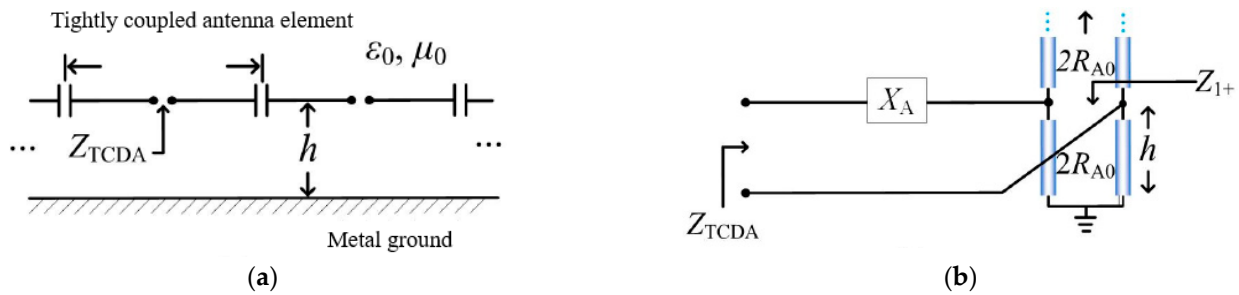


Figure 1. Equivalent circuit of a tightly coupled antenna element: (a) an infinitely large tightly coupled antenna array; (b) the equivalent circuit diagram of the tightly coupled antenna element in an infinitely large array.

Since $2R_{A0}$ and Z_{1+} on the antenna plane are in parallel, $2R_{A0} \parallel Z_{1+}$ exhibits inductance at low frequencies and capacitance at high frequencies. Since the end of the dipole antenna is loaded with capacitance, jX_A shows pure capacitance at low frequencies and pure inductance at high frequencies. When jX_A is connected in series with $2R_{A0} \parallel Z_{1+}$, X_A can be canceled as the imaginary part of $2R_{A0} \parallel Z_{1+}$. Therefore, tightly coupled dipole arrays can usually achieve a bandwidth of more than four times that of the frequency band, as shown in Figure 2.

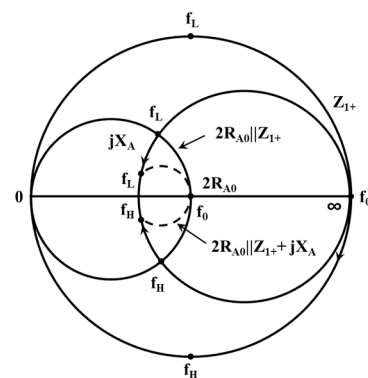


Figure 2. Tightly coupled dipole arrays usually achieve a bandwidth of more than 4 times that of the frequency.

According to the principles above, we designed a conformal antenna that can be implemented using complex printing media, based on the 3-D printing technique. The printing media includes the support medium and radiation function layer, etc., in its structure. The antenna’s radiating elements were printed on the surface of the support material. In a space of about one half-wavelength, we used a conventional array layout to form a conformal structure. A bow-tie-shaped dipole was used as the basic element, as shown in Figure 3, including two pairs of vertically polarized and horizontally polarized dipole elements; the widest element size is $W1$, the narrow side size is $W4$, the total dipole size is $W2$, the inter-element spacing is $D1$, and the feed-point spacing is $W2$. The size of these dimensions would later be checked and optimized.

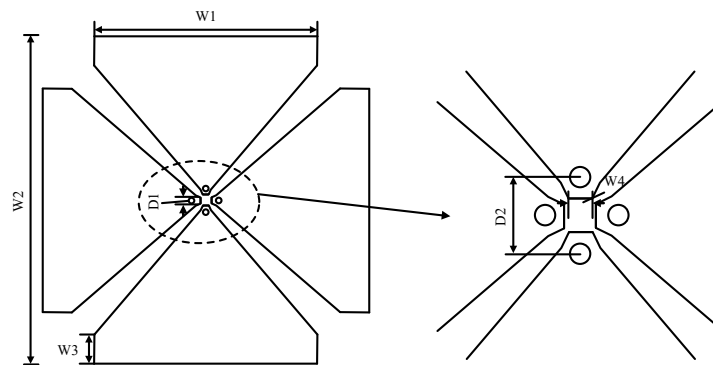


Figure 3. Two pairs of bow-tie-shaped symmetrical radiation objects with a geometric structure are used in a tightly coupled antenna array element.

Since the antenna array is a periodic structure, the element shape is first designed to ensure that a 2-D plane is filled by translational replication. In general, the outer frame of the tightly coupled array is taken as a regular shape, and specific cells are designed within the regular frame. After the outer frame is selected, the element and spacing are determined. The size determines the minimum operating frequency of the array, the spacing is generally related to the array gate flap, and the selection of the appropriate cell spacing is related to the mutual coupling, which affects the key performance of the tightly coupled array. Then, we determine the shape of the element; because the tightly coupled antenna array is a non-resonant structure, the shape can be both bow-tie-shaped and broadband. At present, four kinds of basic elements are commonly used: the connected vibration type, oscillator type, slot slit type, and bow-tie shape.

From the analysis above, it can be seen that the bow-tie-shaped symmetrical radiation element can meet the technical requirements of this project, such as the conformal shape. The final structure of the designed antenna element is shown in Figure 3. At this point, we need to verify the design.

3. Simulation and Size Optimization of the Antenna Element

To check the performance of the designed antenna array element above, this section mainly uses full-wave simulation software to model and optimize the simulation of a low-scattering structure for a bow-tie patch and the current carrier surface. Combining the electromagnetic parameters, such as the dielectric constant and loss tangent of the 3-D printing medium substrate, the final antenna is shown in Figure 3. A simulation of the radiation pattern is shown in Figure 4 using the HFSS software. The modeling simulation optimization was considered by using the neural network method, and the most similar structural parameters were scanned.

According to the user’s actual needs, the index requirements of the antenna elements are shown in Table 1, where the frequency from high to low is F3, FH, F0, FL, F2, and F1, as listed in the Table. For each bow-tie patch, the simulated $|S_{11}|$, VSWR, and input impedance, as shown in Figure 4, have been obtained by the use of HFSS software.

Table 1. Antenna element performance indexes at six frequencies of application.

	Frequency/GHz	Gain/dB	Horizontal Beamwidth/ ^o	Vertical Beamwidth/ ^o
F1	0.35	−19	90	60
F2	0.8	−13	120	90
FL	0.95	−1.5	70	70
F0	1.05	0	80	75
FH	1.15	0.5	80	80
F3	2.0	3	40	60

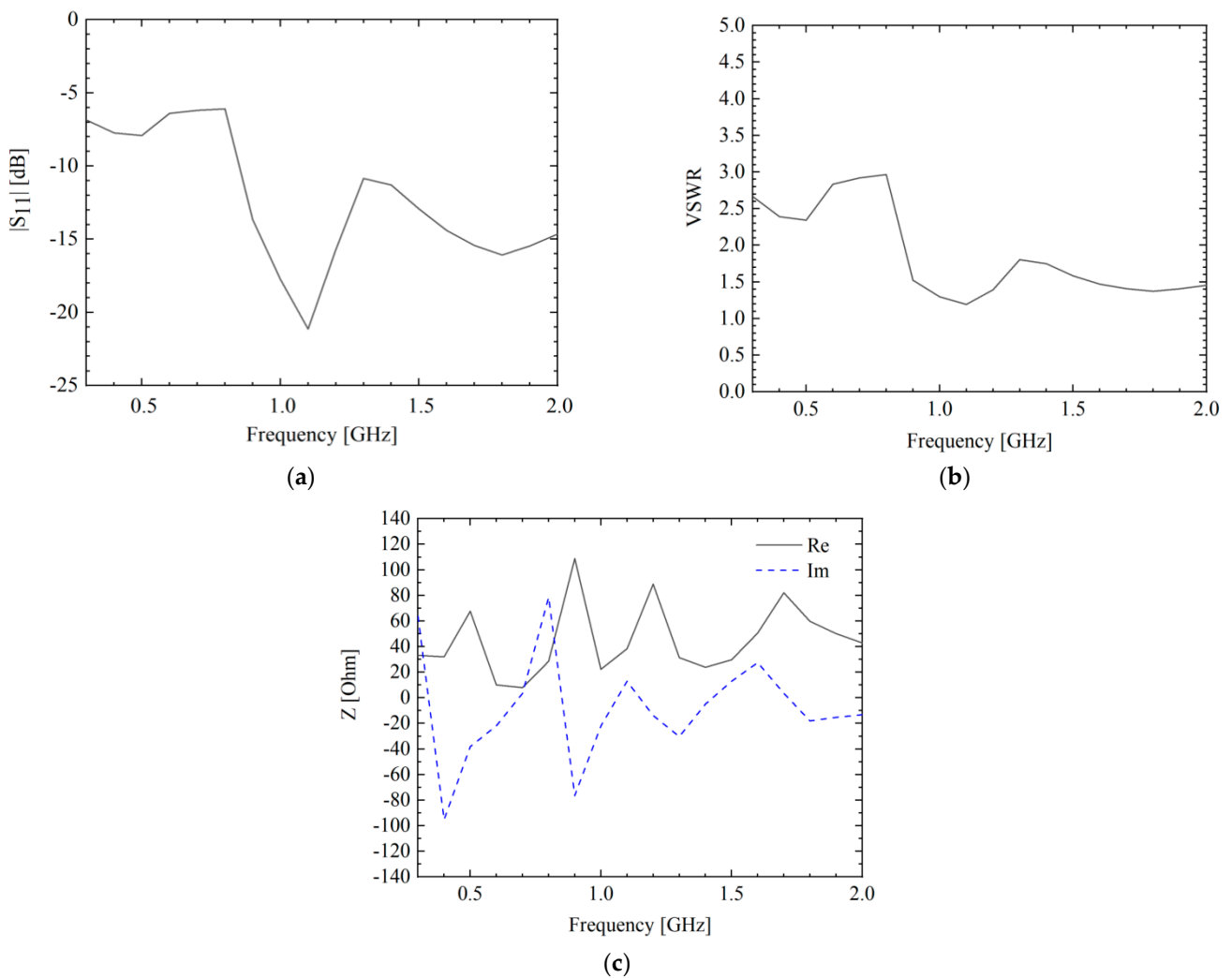


Figure 4. Basic performance of a pair of bow-tie-patch antennas: (a) reflection coefficient, (b) VSWR, and (c) input impedance.

Then, we must check the radiation pattern using the same method, as shown in Figure 5. The curve relates to each frequency point in Table 1. From the figures, the good performance of the antenna array element has been archived. By the way, the radiation patterns of the azimuthal and elevation planes as shown in Figure 5a,b, respectively. In order to improve the radiation efficiency and increase the bandwidth, the element size has been optimized after scanning the frequencies and sizes, and we have obtained the final sizes of the designed antenna element structure, as listed in Table 2. In the following simulation procedure, all the sizes in Table 2 will be used in the array element design.

Table 2. Optimized antenna element with the size of the bow-tie-shaped structure in Figure 3.

Dimensions	W1	W2	W3	W4	D1	D2	D3	D4
Size (mm)	45	65	5.75	1.2	1.75	4	130.6	195

To meet the requirements of the mounted platform, the design of a bow-tie antenna array element uses the normal graphic design process, which can be combined with metal powder coating print technology. Initially, a feeding network was not considered. After the dielectric substrate was designed, it was fabricated by the fused deposition modeling (FDM) technology for processing in the 3-D printer. Then, the antenna array is formed

conformal to the substrate by using the microdroplet injection molding (MIM) technology. The detailed process will be discussed in the next section.

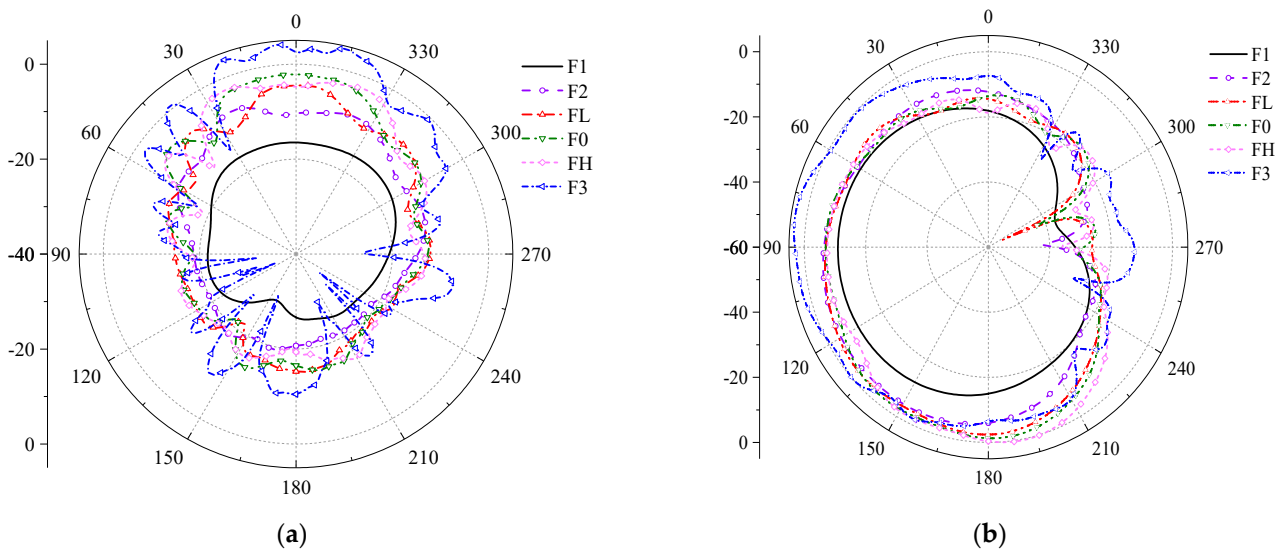


Figure 5. Simulated radiation patterns of the bow-tie-shaped antenna element at the required frequency point, in the (a) azimuthal plane; and (b) elevation plane.

4. Manufacturing Technologies Based on FDM and MIM

4.1. Dielectric Substrate Material

The dielectric substrate is made of high-temperature-resistant SLA photosensitive resin, called JS-UV-LY02-G, which is a low-viscosity translucent material. The machine parts manufactured from this material can bear 100~150 °C temperature for a long period. It can withstand an instantaneous temperature of even 200 °C. Therefore, the material has good dimensional stability and detailed reproduction and can be used for making model hand plates and accessories that require temperature resistance and that are suitable for manufacture by an industrial 3D printer with a 355-nm laser source. Some of the surface, optical, and mechanical parameter properties of JS-UV-LY02-G are shown in Tables 3 and 4, respectively. We used the material for our main antenna substrate design.

In Table 3, the laser source can be controlled according to requirements. For some materials, such as metal with a higher melting point, we must choose a higher pulse probability to meet its printing demands.

Table 3. Surface and optical characteristics of JS-UV-LY02-G.

Surface Properties		Optical Properties		
Appearance	Translucent	Ec	11.3 mJ/cm ²	Critical exposure
Viscosity	340 cps@30 °C	Dp	0.115 mm	Transmission depth: depth of cure vs. slope of Ln(E) curve
Density	1.14 g/cm ³	Build layer thickness	0.1 mm	

Table 4. Mechanical properties of JS-UV-LY02-G Post UV curing.

Test Project	Test Method	Value	Test Method	Value
Tensile strength	ASTMD 638	65 MPa	GB/T1040.1-2006	71 MPa
Elongation at break	ASTMD 638	3~5%	GB/T1040.1-2006	3~5%
Bend strength	ASTMD 790	110 MPa	GB/T9341-2008	115 MPa
Bending modulus	ASTMD 790	2720 MPa	GB/T9341-2008	2850 MPa

Table 4. Cont.

Test Project	Test Method	Value	Test Method	Value
Cantilever beam notched impact strength	ASTMD 256	20 J/m	GB/T1843-2008	25 J/m
Shore hardness	ASTMD 2240	87 D	GB/T2411-2008	87 D
Glass transition temperature	DMA $\tan\theta$ peak	135 °C	/	/
Thermal expansion coefficient (25~50 °C)	ASTME831-05	50 $\mu\text{m}/\text{m}^\circ\text{C}$	GB/T1036-89	50 $\mu\text{m}/\text{m}^\circ\text{C}$
Thermal expansion coefficient (20~100 °C)	ASTME831-05	150 $\mu\text{m}/\text{m}^\circ\text{C}$	GB/T1036-89	160 $\mu\text{m}/\text{m}^\circ\text{C}$

4.2. FDM Hardware System

The FDM hardware system is composed of a mechanical system and a control system. A five-axis piece of 3D printing equipment, a 3D printer with integrated structure and function (Stratasys Objet 260 Connex1) developed by the Key Laboratory of Electronic Equipment Structure Design of the Ministry of Education of Xidian University to realize large-sized-area high-precision flexible circuit printing, which can be applied to touch screens, flexible photovoltaic, flexible OLED display/lighting, frequency-selective surfaces, conformal antennas, and RFID. The ink is compatible with several printheads, such as the Epson DX5 and DX7, the Fuji Starlight and Spectra series, the Konica KM512i and KM1024i, and the Ricoh Gen5, Gen5s, and Gen6 printheads. The performance of the samples, printed with different printheads and conductive inks, was tested, and the results are shown in Table 5.

Table 5. Printing performance of different printheads and conductive inks.

Test Item	BroadCON-INK550	BroadCON-INK550_KM	BroadCON-INK550_RH
Nozzles	Epson full series	Konica 512 i, 1024 i-series	Ricoh GEN5, GEN6
Silver powder particle size/nm	30~50	30~50	30~50
Viscosity/cp	5~6	~12	~10
Silver content/wt%	25~30	35~40	35~40
Square Resistance/ $\text{m}\Omega/\text{mil}^2$	*1~2	*1~2	*1~2
Adhesion	0 level (100% No dislodging)	0 level (100% No dislodging)	0 level (100% No dislodging)
Hardness/H	2	2	2

*: Affected by curing conditions

The mechanical system is composed of the motion, nozzle, forming chamber, material chamber, and other elements, which are mostly of a modular design; each element is independent of the others. The control system consists of a control cabinet and a power cabinet, which is used to control the movement of the nozzle and the temperature of the forming chamber, etc. The structure of the substrate to be printed out in our study is shown in Figure 6a. To reduce the weight of the substrate and to ensure its dielectric properties, the interlayer between the two parabolic surfaces of the substrate is designed as a hollow structure with interconnected microscopic rods. Along with the FDM printer in Figure 6a, the printed substrate is shown in Figure 6b.

From Figure 6b, it can be seen that the dielectric substrate is designed to meet the mounted platform. Its dimensions are listed in Table 6:

L: the length of the substrate;

W: the width of the substrate;

H: the height of the substrate;

h: the distance between the vertex of two curved surfaces;

Ra: the minimum curvature of the curved surface;

Rb: the minimum curvature of the curved surface.

The maximum size of fit for the 7 elements in the horizontal direction is limited by the size of the printer; the conformal antenna array will be fabricated on the substrate. The technological processes will be discussed in detail in the next section.



Figure 6. Three-dimensional printing device and dielectric material: (a) FDM printer; (b) printed substrate.

Table 6. Dimensions and size of the dielectric substrate in Figure 6b.

Dimension	L	W	H	h	Ra	Rb
Size (mm)	480	195.1	131.9	65.6	43.5	81.3

4.3. MIM of the Conductive Patterns

In order to use the inkjet printing technology more successfully for the fabrication of metal film antenna structures, the dimensional resolutions and metal conductivities are essential to address the constraints of this fabrication method. The Stratasys Objet 260 Connex1 3-D printer has been used to inkjet-print the dielectric material. The dielectric material used by the printer is a photosensitive polymer known as VeroBlackPlus. The material has a dielectric constant of 2.6 and a loss tangent of 0.023. The printer has a layer resolution of 16 μm . In order to determine the lateral x - y resolution of the 3-D printer, narrow strips, and gaps are printed, as shown in Figure 7. This information is important for the realization of structures, as dimensions become critical, especially at higher frequencies. It is evident that the printer can reliably print features with widths and gaps of around 300 μm . This resolution is sufficient for the fabrication of microwave components.

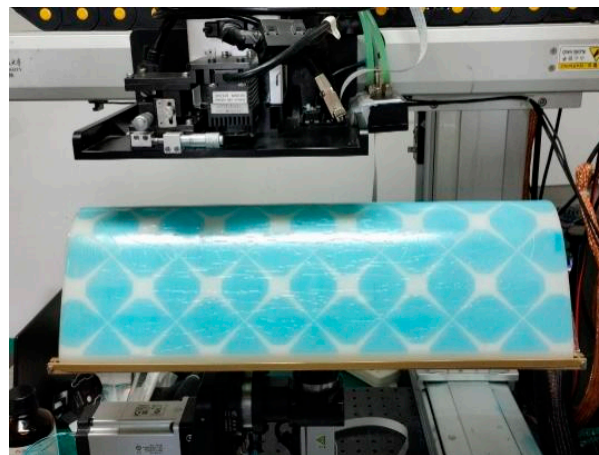


Figure 7. The designed antenna on the fabricated platform.

For the inkjet printing of metal, the Dimatix 2831 materials printer has been used. A commercial silver nanoparticle-based ink from Sigma Aldrich (product 719048) with an average particle size of 150 nm has been printed to form metal tracks on the 3-D printed dielectric. As inkjet printing is highly dependent on the substrate type, it is necessary to characterize the ink on a particular substrate in order to obtain an accurate measure of the printing performance. Before printing, it is necessary to treat the surface of the substrate with acetone in order to remove unwanted contaminants, such as grease and oils. The metal lines and gaps are inkjet-printed with a 20- μm -drop spacing and a 1-pL-drop volume cartridge. As is made clear in the image, a minimum line width of around 23 μm and gaps as narrow as 15 μm are realizable using inkjet printing. The surface of the inkjet-printed traces is slightly rough, as can be seen in Figure 6b; this is due to the roughness of the 3-D printed substrate. The measured root-mean-square roughness is 6.4 μm . The conductivity of the metal traces is critical for the performance of RF components.

The printed traces are subjected to heat so that the nanoparticles fuse together to form continuous metal tracks. This process is termed sintering. The conductivity of the metal traces increases with the duration of the sintering and temperature. In addition, more layers can be printed to achieve higher conductivities. The resistance decreases by printing more layers and also by increasing the sintering duration. A minimum sheet resistance of around 1.3 Ω/sq . is achieved by printing 10 layers of silver ink, giving a conductivity of around $3.8 \times 10^5 \text{ S/m}$.

To ensure the stability of the conformal antenna-forming performance and accuracy, the conductive pattern was printed on the media substrate before printing a layer of blue UV light-curing resin as a substrate material. Here the GH2220 nozzle's special blue UV ink, which can be printed directly onto various types of coated paper, white card, gray-background white board, PVC card, and other materials, fast drying speed, and a printing speed of between 30 and 100 m/h. The product performance offers much more stability, without clogging the nozzle, and a good drying speed, diffusion, chromaticity, etc. This ink has a strong waterproof function that is especially suitable for printing without varnishing and without lamination products. The ink diameter is less than 1 μm ; the ink does not contain volatile organic solvents and has an ultra-low viscosity and no irritating odor, and the ink can be used in the printing process without blocking the nozzle. The long-term high-temperature storage test shows no pigment coalescence, sinking, layering, or other abnormal phenomena, and can be matched with the various models of UV digital printing systems on the market. After curing, the ink layer gains a high level of hardness, yielding good adhesion, scrub resistance, solvent resistance, and high gloss; the finish can also be customized without gloss, and has a high level of sunlight resistance.

The UV ink and weak solvent ink, according to their own nature, determine their respective application methods and eventual applications. In terms of structure, the biggest difference between UV inks and traditional solvent inks is, firstly, that they contain little or no volatile solvents (VOCs). Traditional solvent-based inks contain at least 50% of volatile solvents, which is the essence of UV inks being considered environmentally friendly inks. Secondly, UV inks are generally composed of 30–40% of the main resin, 20–30% of the active monomer, and a small amount of photoinitiators and similar leveling agents, defoamers, and other additives. Among them, the main resin and the active monomer are reactive. The inkjet printout is also shown in Figure 7.

5. Feed Structure Design

According to the system function requirements of the array, the structure-function integration design of the electrical transmission element and the radiation element of the array are carried out, with the factors of electrical transmission, interface matching, and line-forming being the constraint requirements, with common design optimization tools such as CAD/CAE/CAPP being used to realize the high integration of structure and function needed in the limited space available. The cable assembly is inserted into the antenna structure matrix through its side guide structure, and the solder pins are aligned

with the antenna matrix opening. Then, four solder pins are welded and filled and are fixed with potting material after the commissioning is complete, as shown in Figure 8. The number of elements is N , the distance is d , and the uniform linear array is arranged along the y -axis direction, where the electric field intensity in the far zone of the i th element is E_i , yielding:

$$E_i = K_i I_i f_i(\theta, \varphi) \frac{e^{-j2\pi r_i/\lambda}}{r_i} \tag{4}$$

where I_i indicates the fed current amplitude of the i th antenna element and $I_i = a_i e^{-ji\Delta\phi_B}$, a_i is the weighting factor amplitude, $f_i(\theta, \varphi)$ is the radiation pattern of the element, $\Delta\phi_B$ is the phase difference between the i th element and the first, and r_i is the distance between the center of the antenna and the observing point.

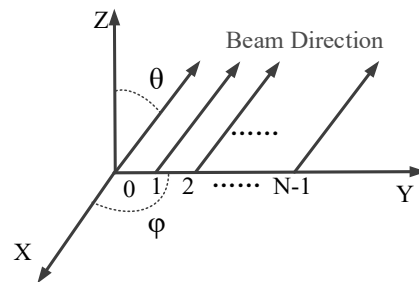


Figure 8. N-element linear array, with the main beam pointing in the negative x -direction on the x - y plane.

The total field of the main beam can be expressed by:

$$E = \sum_{i=0}^{N-1} E_i = \sum_{i=0}^{N-1} K_i I_i f_i(\theta, \varphi) \frac{e^{-j\frac{2\pi}{\lambda} r_i}}{r_i} \tag{5}$$

For the uniform linear array, the amplitude of the fed current is the same level; therefore, we have:

$$E = K f(\theta, \varphi) \sum_{i=0}^{N-1} a_i e^{-ji\Delta\phi_B} \frac{e^{-j\frac{2\pi}{\lambda} r_i}}{r_i} \tag{6}$$

where $r_i = r_0 - id\cos\alpha_y$ and $\cos\alpha_y = \sin\theta\sin\varphi$. When $K = 1$, we have:

$$E(\theta, \varphi) = f(\theta, \varphi) \sum_{i=0}^{N-1} a_i e^{-j(\frac{2\pi}{\lambda} id\sin\theta\sin\varphi - i\Delta\phi_B)}. \tag{7}$$

From Equation (7), it can be seen that the total radiation pattern of the array is composed of the multiplication of the element pattern and the array factor, where $f(\theta, \varphi)$ represents the antenna element pattern and the right part is the array factor. If each element is an omnidirectional antenna, then $f(\theta, \varphi) = 1$, and we have:

$$F(\theta) = \sum_{i=0}^{N-1} a_i e^{ij(\frac{2\pi}{\lambda} d\sin\theta - \Delta\phi_B)} \tag{8}$$

where $\Delta\phi_B = \frac{2\pi}{\lambda} d\sin\theta_B$, θ_B is an angle between the main beam and z -axis, $\Delta\phi = \frac{2\pi}{\lambda} d\sin\theta$ is the phase difference between each element. If $\Delta\phi - \Delta\phi_B = X$, we have:

$$F(\theta) = \frac{1 - e^{jNX}}{1 + e^{jX}}. \tag{9}$$

Then, we have:

$$F(\theta) = \left(\frac{\sin \frac{NX}{2}}{\frac{NX}{2}} \right) e^{j\frac{N-1}{2}X} \tag{10}$$

In our design, where $N = 7$, we have:

$$|F(\theta)| = N \left(\frac{\sin \frac{NX}{2}}{\sin \frac{X}{2}} \right) = N \frac{\sin \frac{Nd\pi}{\lambda} (\sin\theta - \sin\theta_B)}{\frac{Nd\pi}{\lambda} (\sin\theta - \sin\theta_B)} \quad (11)$$

From the discussion above, we designed seven feed sources to meet the user's requirements, as shown in Figure 9.

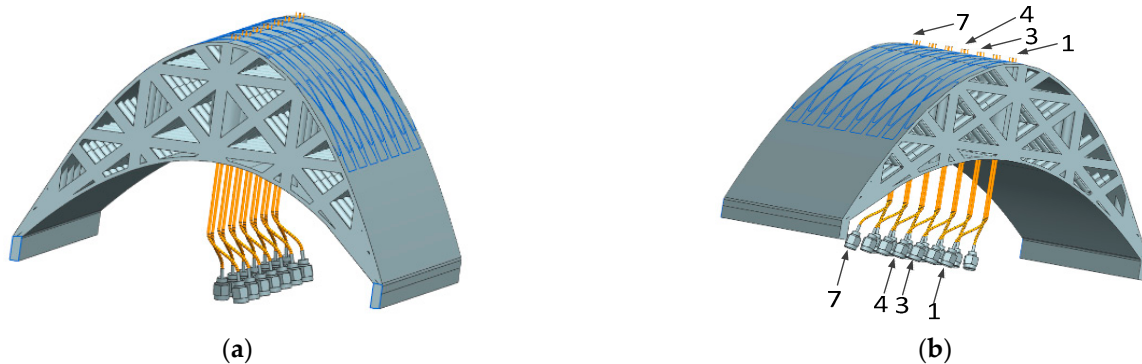


Figure 9. The cable assembly inserted into the antenna array structure through its side guide structure: (a) main view; and (b) solder pins aligned with the antenna array opening. Seven ports are symmetrically distributed in order.

The antenna has been manufactured using a combination of 3-D inkjet printing of dielectric and 2-D inkjet printing of metal. The helical structure, along with the lens, has been monolithically manufactured using a 3-D inkjet printer. This shows one major advantage of 3-D printing, as complex structures can be fabricated rapidly via the precise layer-by-layer deposition of material through a digitally controlled process. The print time for this 3-D geometry was 5 h 21 min with the available printer.

An industrial-grade printer will take 40% less time to print the same geometry. The same metallization geometry has been used in the simulation, and this does not have a significant effect on the antenna performance. For mechanical support, two vertical posts have also been attached to the support after the metallization of the bow-tie array as shown in Figure 10, which rest on the ground plane. The ground has been inkjet-printed separately because of the inkjet printer's limited work area, which cannot accommodate the complete structure. However, this will not be an issue if larger printers with more work volume are used. After attaching the ground plane, the SMA connector is mounted onto the antenna array for measurements.

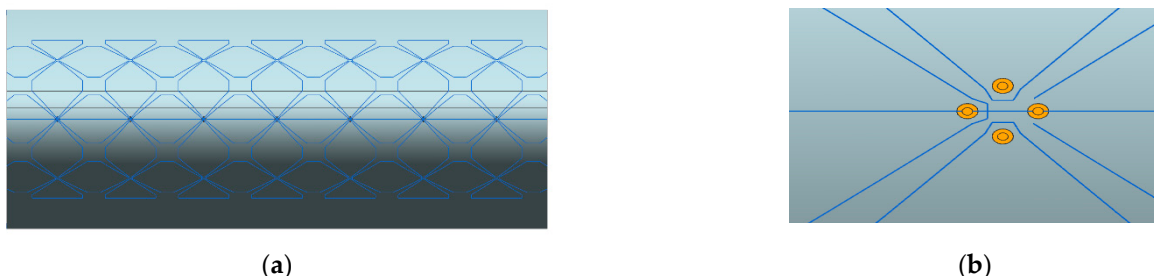


Figure 10. Cable assembly inserted into the antenna array structure location: (a) top view from the conformal antenna side; (b) local view of one antenna element's feed point.

6. Experiment and Design Method Verification

To verify our design, the reflection coefficient and isolation between neighboring elements have been tested. The results are depicted in Figure 11. The radiation pattern of the proposed antenna array has also been tested in our microwave anechoic chamber.

Figure 12 shows the fabricated prototype and the testing scenario. Because the pattern was implemented in the H-plane, the array has little influence on the E-plane. Therefore, only the H-plane needs to be measured and analyzed. The simulation and measurement results of the radiation patterns in the H-plane are presented in Figure 13; the simulation results are consistent with the measurement results at 0.35 GHz, 0.8 GHz, 0.95 GHz, 1.05 GHz, 1.15 GHz, and 2.0 GHz. Therefore, the proposed antenna array can cover the aviation and BeiDou navigation bands. Even at 300 MHz, especially in the case of the rescue band, the measurement results of the radiation patterns are in very good agreement with the simulation.

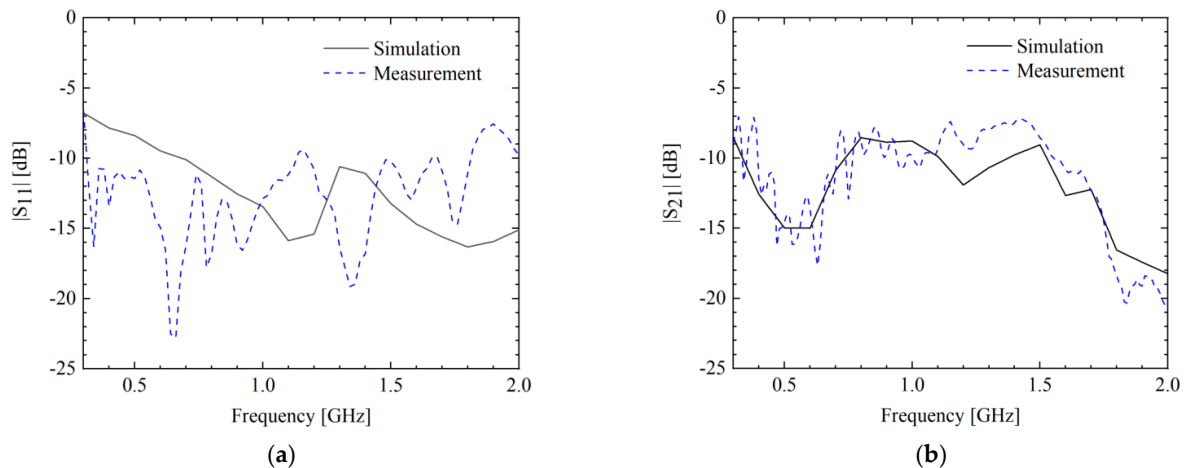


Figure 11. Performance of the antenna array: (a) reflection coefficient; (b) isolation between the neighboring elements.



Figure 12. Test setup in the microwave anechoic chamber; the z-axis points to the top of the antenna.

As shown in Figure 12, we have obtained good results in our laboratory. The microwave anechoic chamber is a spherical far-field testing system, with a far-field distance of 8 m, a frequency testing range of 300 MHz–18 GHz, a static zone size of 1.8 m, and a repetition error of ± 0.5 dB.

The antenna array is designed with a total of 8 main ports. In order not to lose generality, the edge units and intermediate units are selected as typical units for testing. Here, we chose units 1, 3, and 4, as shown in Figure 9b, to record the testing results shown in Figures 13 and 14.

In the Figures, the received electric field is used for the radiation pattern in the microwave anechoic chamber test and mainly shows the vertical polarization. The horizontal polarization unit is long-lasting, and its radiation characteristics are similar to those of a conventional tightly coupled antenna. The vertical polarization unit spends a short period in the elevation plane. Therefore, the radiation characteristics of the vertical polarization unit are mostly verified. Then, we depicted the vertical polarization pattern in the elevation plane, as shown in Figure 14.

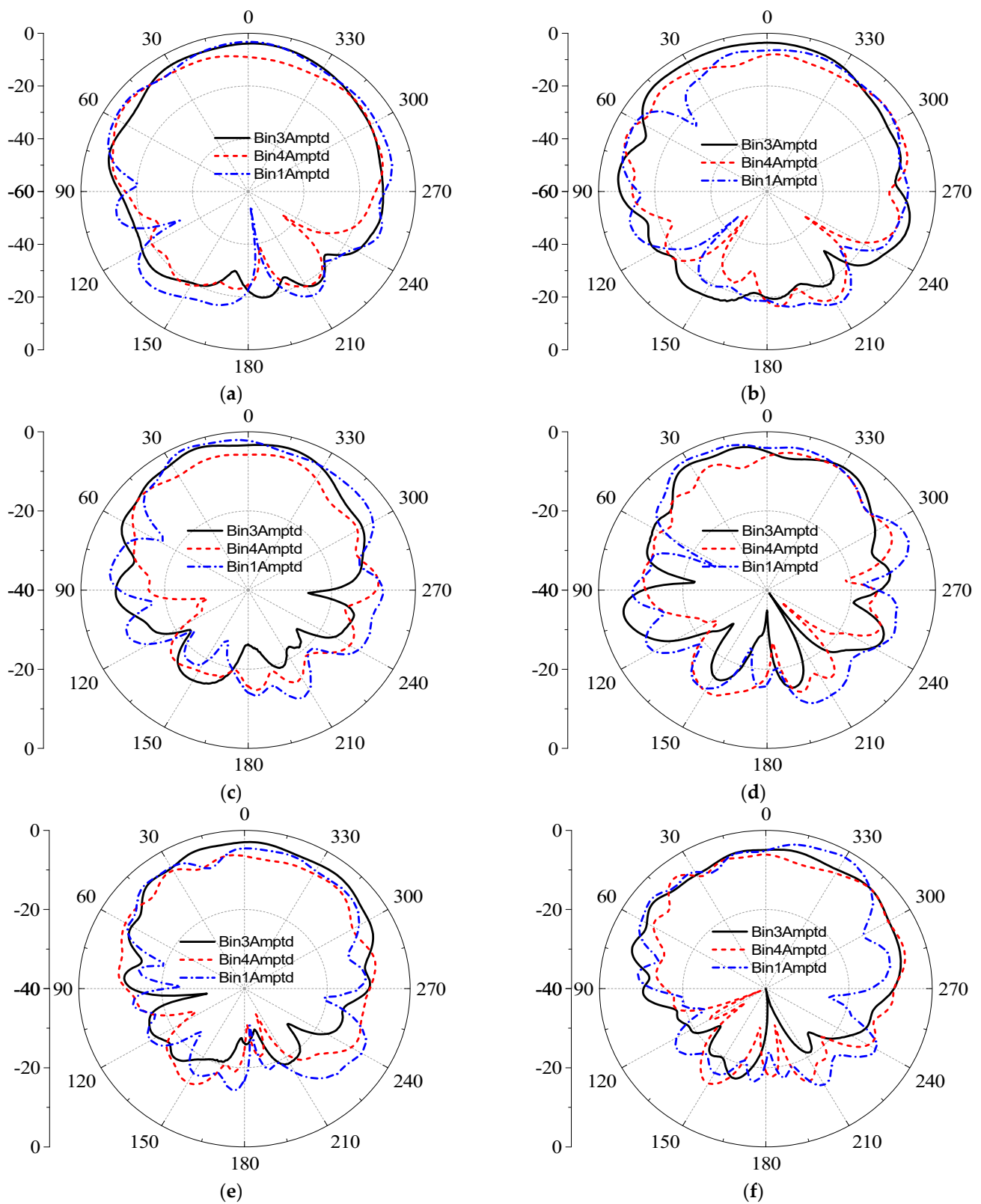


Figure 13. Experiment radiation pattern on the horizontal plane for (a) 0.35 GHz; (b) 0.8 GHz; (c) 0.95 GHz; (d) 1.05 GHz; (e) 1.15 GHz; and (f) 2.0 GHz.

Other elements of the antenna array have been tested using the same method. To save space, the results are not listed here. In fact, the above results are sufficient to illustrate that

3D printing technology has obvious advantages in realizing the design and manufacturing of conformal tightly coupled antennas.

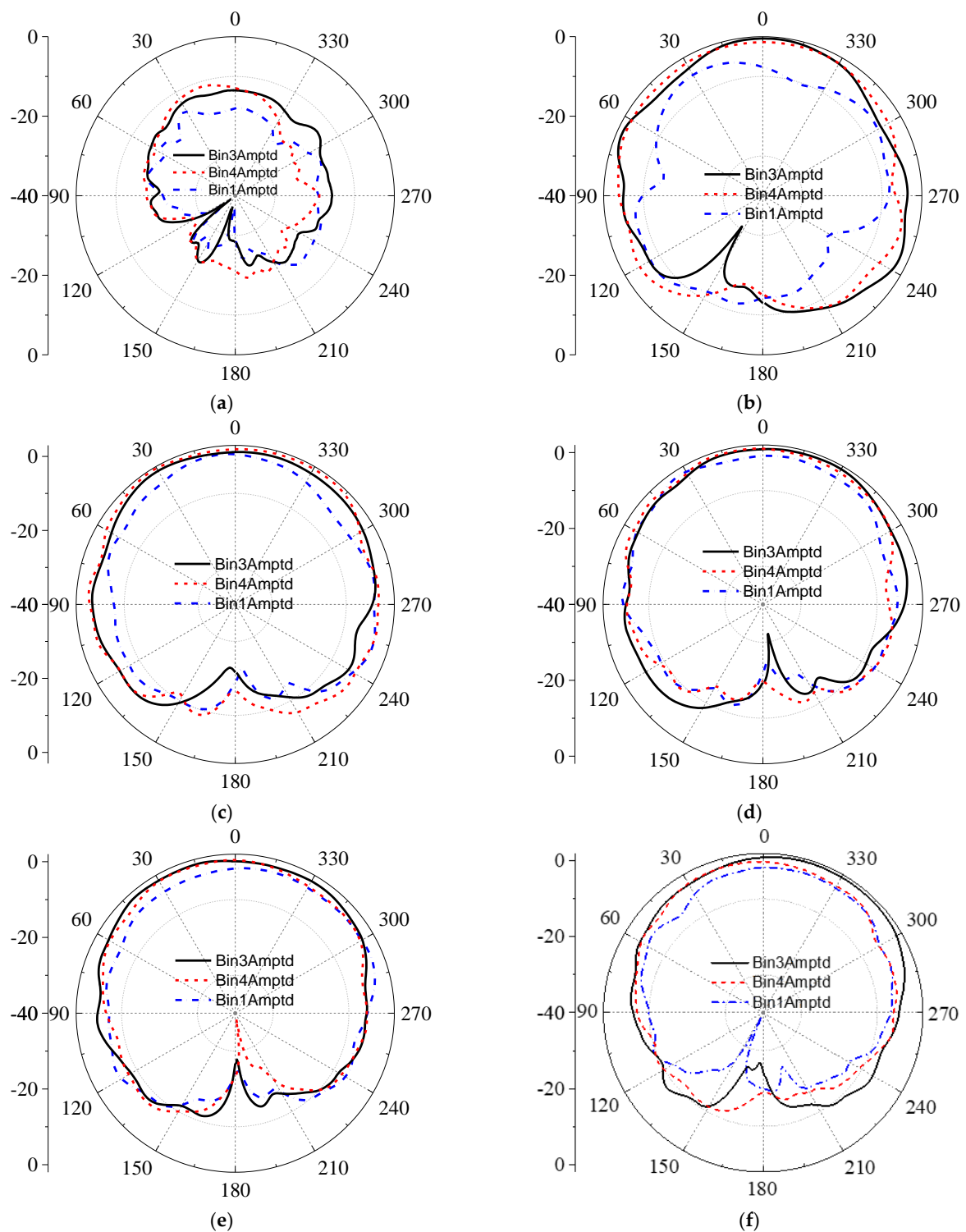


Figure 14. Experiment radiation patterns at an elevation plane for the frequency: (a) 0.35 GHz; (b) 0.8 GHz; (c) 0.95 GHz; (d) 1.05 GHz; (e) 1.15 GHz; and (f) 2.0 GHz.

7. Conclusions

This approach mainly focuses on the application of 3-D printing technology in conformal antennas, which proves that conformal antennas based on the principle of tight

coupling can be designed and printed using the current printing technology. With the increase in printing materials and layers, on the basis of this paper, we will continue to study the structural bearing characteristics of printing materials on conformal antennas and the impact of different materials on electrical performance parameters. Increasing the number of layers can expand the antenna bandwidth and optimize the electrical performance of the antenna, laying a foundation for the rapid processing of complex structure antennas in the future. Combining design with 3-D printing technology, we simulated and designed a tightly coupled ultra-wideband conformal antenna and completed the printing of a substrate and radiators. The measurement results are shown to be in very good agreement with the simulation. Through conformal antenna processing, 3-D printing technology gives us very good application prospects. In this work, a bow-tie antenna array was monolithically integrated with a dielectric substrate. This integration has resulted in a conveniently fabricated airborne antenna. This work shows the utility of additive printing technologies to realize complex 3-D RF components that are otherwise very difficult and expensive to realize using conventional manufacturing techniques.

Author Contributions: Conceptualization, L.H. and H.Z.; methodology, L.H.; validation, L.H., W.J. and P.Z.; formal analysis, W.T.; investigation, L.H.; resources, T.D.; data curation, L.Z.; writing—original draft preparation, L.H.; writing—review and editing, H.Z.; visualization, G.W.; supervision, G.W. and L.Z.; project administration, H.Z.; funding acquisition, T.D. and H.Z. All authors have read and agreed to the published version of the manuscript.

Funding: This work is supported by the National Natural Science Foundation of China and the Key Research and Development Project of Hebei Province under Grants 62071166 and 21310401D, respectively.

Conflicts of Interest: The authors declare no conflict of interest.

References

1. Paulsen, J.A.; Renn, M.; Christenson, K.; Plourde, R. Printing conformal electronics on 3D structures with aerosol jet technology. In Proceedings of the Future of Instrumentation International Workshop (FIIW), Gatlinburg, TN, USA, 8–9 October 2012; pp. 1–4.
2. Munk, B.; Taylor, R.; Durharn, T.; Croswell, W.; Pigon, B.; Boozer, R.; Brown, S.; Jones, M.; Pryor, J.; Ortiz, S.; et al. A low-profile broadband phased array antenna. In Proceedings of the IEEE Antennas and Propagation Society International Symposium, Columbus, OH, USA, 22–27 June 2003; Volume 2.
3. Zhao, M.Y.; Zhu, Y.J.; Wang, T.; Li, T.P.; Xiao, B.L.; Niu, F.L.; Lei, X. A wideband scanning circularly polarized array antenna based on the shorted transmission line model. *IEEE Access* **2022**, *10*, 78493–78501. [[CrossRef](#)]
4. Jones, M.; Rawnick, J. A new approach to broadband array design using tightly coupled elements. In Proceedings of the IEEE Military Communications Conference, Orlando, FL, USA, 29–31 October 2007; pp. 1–7.
5. Xiao, S.; Yang, S.; Chen, Y.; Qu, S.-W.; Hu, J. An ultra-wideband tightly coupled dipole array co-designed with low scattering characteristics. *IEEE Trans. Antennas Propag.* **2018**, *67*, 676–680. [[CrossRef](#)]
6. Kasemodel, J.A.; Chen, C.-C.; Volakis, J.L. Wideband planar array with integrated feed and matching network for wide-angle scanning. *IEEE Trans. Antennas Propag.* **2013**, *61*, 4528–4537. [[CrossRef](#)]
7. Wang, J.; Zhao, X.; Ye, Y.; Liu, S. A millimeter-wave ultra-wideband tightly coupled dipole array antenna for vehicle communication. *IEEE Antennas Wirel. Propag. Lett.* **2022**; early access. [[CrossRef](#)]
8. Zhang, H.; Yang, S.; Xiao, S.W.; Chen, Y.; Qu, S.W.; Hu, J. Ultra-wide band phased antenna arrays based on tightly coupled open folded dipoles. *IEEE Antennas Wirel. Propag. Lett.* **2019**, *18*, 378–382. [[CrossRef](#)]
9. Wang, J.; Cui, W.; Zhou, Y.; Liu, R.; Wang, M.; Fan, C.; Zheng, H.; Li, E. Design of wideband antenna array with dielectric lens and defected ground structure. *Electronics* **2021**, *10*, 2066. [[CrossRef](#)]
10. Xing, H.; Wang, X.; Gao, Z.; An, X.; Zheng, H.-X.; Wang, M.; Li, E. Efficient isolation of an MIMO antenna using defected ground structure. *Electronics* **2020**, *9*, 1265. [[CrossRef](#)]
11. Kim, M.-S.; Chu, W.-S.; Kim, Y.-M.; Avila, A.P.G.; Ahn, S.-H. Direct metal printing of 3D electrical circuit using rapid prototyping. *Int. J. Precis. Eng. Manuf.* **2009**, *10*, 147–150. [[CrossRef](#)]
12. Gjokaj, V.; Papapolymerou, J.; Albrecht, J.D.; Wright, B.; Chahal, P. A compact receive module in 3-D printed Vivaldi antenna. *IEEE Trans. Compon. Packag. Manuf. Technol.* **2019**, *10*, 343–346. [[CrossRef](#)]
13. Tzanidis, I.; Sertel, K.; Volakis, J.L. UWB low-profile tightly coupled dipole array with integrated balun and edge terminations. *IEEE Trans. Antennas Propag.* **2013**, *61*, 3017–3025. [[CrossRef](#)]
14. Zhou, L.; Tang, M.; Mao, J. 3-D printed Vivaldi antenna fed by SIW slot for millimeter-wave applications. In Proceedings of the 2021 IEEE International Conference on Microwave and Millimeter Wave Technology, Nanjing, China, 23–26 May 2021; pp. 1–3. [[CrossRef](#)]

15. Holland, S.S.; Schaubert, D.H.; Vouvakis, M.N. A 7–21 GHz dual-polarized planar ultrawideband modular antenna (puma) array. *IEEE Trans. Antennas Propag.* **2012**, *60*, 4589–4600. [[CrossRef](#)]
16. Olivová, J.; Popela, M.; Richterová, M.; Štefl, E. Use of 3D printing for horn antenna manufacturing. *Electronics* **2022**, *11*, 1539. [[CrossRef](#)]
17. Agarwal, S.; Masotti, D.; Nikolaou, S.; Costanzo, A. Conformal design of a high-performance antenna for energy-autonomous UWB Communication. *Sensors* **2021**, *21*, 5939. [[CrossRef](#)] [[PubMed](#)]
18. He, Y.; Oakley, C.; Chahal, P.; Albrecht, J.; Papapolymerou, J. Aerosol jet printed 24 GHz end-fire quasi-Yagi-Uda antenna on a 3-D printed cavity substrate. In Proceedings of the 2017 International Workshop on Antenna Technology: Small Antennas, Innovative Structures, and Applications (iWAT), Athens, Greece, 1–3 March 2017; pp. 1–4.
19. Sifat, S.M.; Ali MM, M.; Shams, S.I.; Sebak, A.R. High gain bow-tie slot antenna array loaded with grooves based on printed ridge gap waveguide technology. *IEEE Access* **2019**, *7*, 36177–36185. [[CrossRef](#)]
20. Muth, J.T.; Vogt, D.M.; Truby, R.L.; Mengüç, Y.; Kolesky, D.B.; Wood, R.J.; Lewis, J.A. Embedded 3D printing of strain sensors within highly stretchable elastomers. *Adv. Mater.* **2014**, *26*, 6307–6312. [[CrossRef](#)] [[PubMed](#)]
21. Farooqui, M.F.; Shamim, A. 3-D inkjet-printed helical antenna with integrated lens. *IEEE Antennas Wirel. Propag. Lett.* **2017**, *16*, 800–803. [[CrossRef](#)]